Two-Stage Automatic Mass Balancing and Attitude Control for 3-DoF Spacecraft Attitude Simulators

Yong-Hwan Kim[a,*], Kyungryeung Min[a], Yangchan Cho[a,*]

[a]*Space n Bean Inc., 232 Gongneung-ro, Nowon-gu, Seoul, 01811, Republic of Korea*

Abstract

Three-degree-of-freedom (3-DoF) air-bearing simulators are widely used for ground-based validation of spacecraft attitude determination and control systems. However, residual gravity torques caused by center-of-rotation to center-of-gravity (CR-CG) offsets can degrade simulation fidelity, particularly during coupled three-axis maneuvers. This paper presents a sequential coarse-to-fine automatic mass balancing framework, referred to as the Robust Automatic Mass Balancing Operator (RAMBO), designed to reduce residual CR-CG offsets under mechanical non-orthogonality and cross-axis coupling while maintaining a negative vertical offset for pendulum stability. The framework sequentially applies an active coarse stage (CRAMBO) for rapid offset reduction and a fine stage (FRAMBO) for precise CR-CG offset estimation using free-response motion data collected after platform reinitialization. The final FRAMBO estimate is subsequently used to construct an attitude-dependent gravity-torque feedforward term within a conventional quaternion proportional-derivative (PD) controller for the hardware attitude-control experiment. Hardware experiments demonstrated that the dynamic-equivalent CR-CG offset estimate converged to approximately $[0.08, 0.12, -27.62]$ μm. Based on the onboard VN-100 estimates, the resulting hardware configuration maintained steady-state attitude errors within $\pm 0.5°$ and angular velocity errors within $\pm 0.4°$/s for roll and $\pm 0.2°$/s for pitch and yaw during a coupled diagonal maneuver. A secondary IMU comparison further provided a roll/pitch consistency check rather than an independent ground-truth validation. These results demonstrate the hardware implementation of the

*Corresponding authors.

Email addresses: `kyh@spacenbean.com` (Yong-Hwan Kim), `silence.cho@spacenbean.com` (Yangchan Cho)

two-stage RAMBO procedure and the subsequent use of its final estimate in safety-constrained three-axis attitude-control testing.

Keywords: 3-DoF air-bearing simulator, spacecraft attitude simulator, automatic mass balancing, CR-CG offset estimation, gravity-torque feedforward, batch least-squares estimation

---

1. Introduction

Ground-based attitude simulators are widely used to verify spacecraft attitude determination and control systems (ADCS) prior to on-orbit operation [1–3]. Among them, three-degree-of-freedom (3-DoF) air-bearing simulators provide a nearly frictionless rotational environment, enabling hardware-in-the-loop (HIL) integration of sensors, actuators, and control algorithms [1, 4–10]. Therefore, these simulators serve as experimental platforms for bridging the gap between numerical simulations and practical spacecraft attitude control validation.

A key requirement for accurate ground-based attitude simulation is the alignment between the center of rotation (CR) and the center of gravity (CG) of the floating platform [8, 9, 11]. In a 1-g ground environment, a residual CR-CG offset generates a gravity-induced disturbance torque, which can distort the free rotational response of the simulator, reduce the available actuator margin, and degrade the reliability of attitude control experiments [12, 13]. To mitigate this issue, manual balancing procedures and automatic mass balancing systems using sliding mass mechanisms have been investigated together with estimation algorithms, including least-squares estimation, recursive identification, and Kalman filter-based approaches [3, 8, 9, 14–17].

Despite these efforts, practical hardware limitations remain challenging. Many mass balancing methods are formulated under idealized assumptions, such as orthogonal sliding mass axes, repeatable actuator motion, and time-invariant mass properties [8, 9]. However, non-orthogonal slider configurations can produce coupled relationships between slider displacements and centroid deviation components, indicating that the motion of one slider may affect multiple components of the CR-CG offset [18]. In actual experimental testbeds, similar coupling can also arise from geometric installation errors, assembly tolerances, actuator resolution limits, mechanical repeatability, sensor noise, and unmodeled residual disturbances [3, 13]. These constraints indicate the need for a balancing strategy that can reduce residual offsets under non-ideal hardware conditions rather than relying on a single-stage or purely static calibration procedure.

Another important design constraint is the vertical CR-CG offset. For spherical air-bearing simulators, the ideal zero-offset condition eliminates gravity-induced restoring torque; however, if the CG is located above the rotational center, the platform becomes prone to tipping, whereas a CG below the rotational center produces a pendulum-like restoring motion [11]. In the coordinate convention used in this study, this stable pendulum configuration corresponds to maintaining a slightly negative vertical CR-CG offset. Therefore, the balancing objective is not to force all components of the CR-CG offset to zero, but to reduce the residual gravity disturbance torque while preserving a negative vertical offset for safe platform operation. This remaining offset-induced torque should then be explicitly considered during attitude control experiments.

To address these coupled challenges, this paper presents a two-stage automatic mass balancing system, referred to as the Robust Automatic Mass Balancing Operator (RAMBO), for a hemispherical 3-DoF spacecraft attitude simulator. The proposed RAMBO framework consists of a coarse balancing stage, CRAMBO, which rapidly reduces the initial CR-CG offset, and a fine balancing stage, FRAMBO, which refines the offset estimate through sequential platform reinitialization. This stop-and-restart operation is introduced to reduce the influence of transient dynamic disturbances during the fine estimation phase. The final FRAMBO estimate, $\hat{\mathbf{r}}_{cg}$, is subsequently used to construct an attitude-dependent gravity-torque feedforward term within a conventional quaternion proportional-derivative (PD) controller for the hardware attitude-control experiment [19, 20].

The main contributions of this study are summarized as follows:

- A two-stage automatic mass balancing framework is proposed to reduce estimated residual CR-CG offsets under non-ideal sliding mass mechanisms, while maintaining a negative vertical-offset stability constraint.

- A batch least-squares-based CR-CG offset estimation procedure is integrated with sequential coarse-to-fine estimate-and-correct operation through CRAMBO and FRAMBO.

- The mass-balancing performance of the two-stage RAMBO framework is experimentally validated on a 3-DoF spacecraft attitude simulator equipped with a hemispherical air bearing. The final FRAMBO estimate is then applied as a fixed model parameter for gravity-torque feedforward in a subsequent coupled three-axis hardware maneuver.

The remainder of this paper is organized as follows. Section 2 describes the system configuration and dynamic model of the spacecraft attitude simulator. Section 3 presents the proposed two-stage automatic mass balancing system. Section 4 describes the quaternion PD attitude-control implementation using the final FRAMBO estimate for gravity-torque feedforward. Section 5 presents the mass-balancing validation results and the subsequent hardware attitude-control test results. Section 6 discusses practical limitations and applicability to ground-based ADCS validation. Finally, Section 7 concludes the paper.

2. System Configuration and Dynamic Modeling

2.1. Spacecraft Attitude Simulator Configuration

The experimental platform is a hemispherical air-bearing-based three-degree-of-freedom (3-DoF) spacecraft attitude simulator that permits unrestricted yaw motion and mechanically limits roll and pitch to $\pm 30°$. The air bearing provides nearly frictionless rotation about its center [11], while the mass balancing subsystem reduces the residual gravity torque caused by the CR-CG offset.

The simulator comprises sensing, attitude-control actuation, automatic mass balancing, and processing/communication subsystems. A VectorNAV VN-100 IMU/AHRS provides the primary attitude and angular-rate feedback for control and performance evaluation. Its nominal pitch/roll accuracy is $0.5°$ RMS under static conditions and $1.0°$ RMS under dynamic conditions, with a typical gyroscope in-run bias stability of $5°/h$ [21]. A WITMotion BWT901CL is used only for secondary roll/pitch consistency checks. Three orthogonally mounted reaction wheel assemblies generate the control torques, while the RAMBO sliding-mass mechanism adjusts the platform CG relative to the bearing center. A Raspberry Pi 5 executes the balancing algorithm, attitude controller, actuator commands, and data logging. Figures 1 and 2 show the mechanical configuration and electrical/communication interfaces, respectively.

Tables 1 and 2 summarize the simulator specifications and main hardware components, respectively.

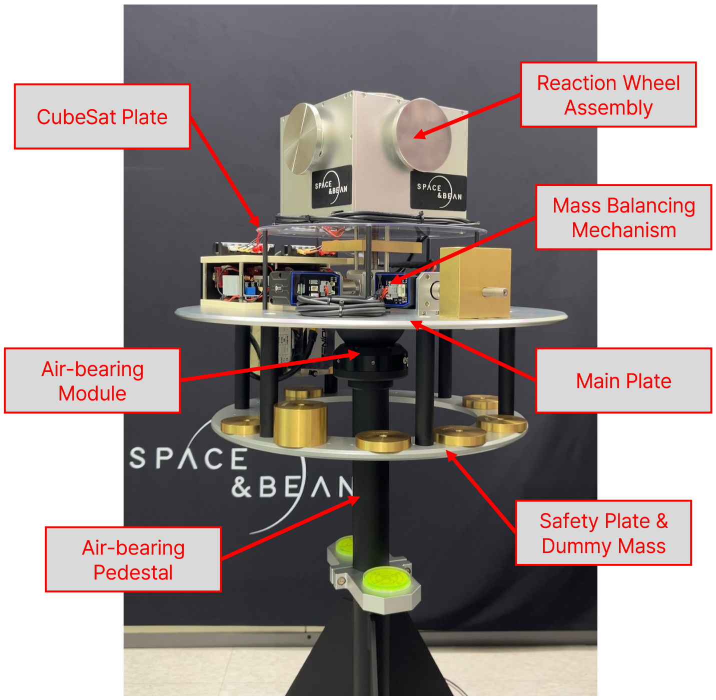

Figure 1: Overall configuration of the 3-DoF spacecraft attitude simulator.

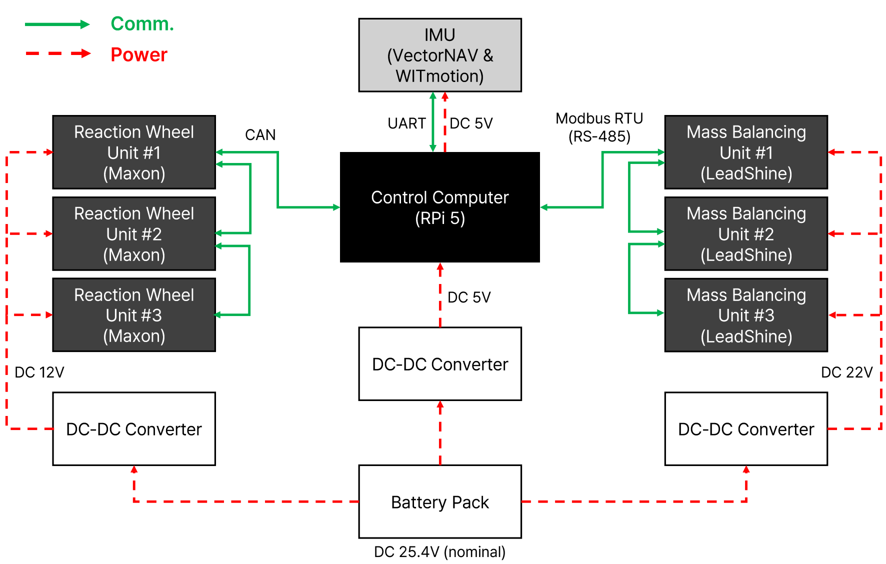

Figure 2: Electrical and communication interface of the 3-DoF spacecraft attitude simulator.

Table 1: Main physical and operational specifications of the 3-DoF spacecraft attitude simulator.

Category	Parameter	Value	Unit
Platform properties	Total floating mass, m_{tot}	26.95	kg
	Roll-axis MOI, J_{xx}	0.612	kg·m^2
	Pitch-axis MOI, J_{yy}	0.684	kg·m^2
	Yaw-axis MOI, J_{zz}	0.668	kg·m^2
	Allowable roll/pitch range	±30	deg
	Allowable yaw range	Unlimited	–
Air bearing	Sphere diameter	100	mm
	Operating pressure	80	psi
Reaction wheel assembly	Rated wheel speed	3000	RPM
	Maximum control torque	48.6	mN·m
	Angular momentum capacity	97.2	mN·m·s
Mass balancing mechanism	Sliding mass, m_x, m_y, m_z	1.5, 1.5, 1.0	kg
	Slider stroke, x and y axes	±32.5	mm
	Slider stroke, z axis	±23.0	mm
	Slider positioning resolution	5.0	µm

Note: The moments of inertia were estimated from the 3D CAD model.

Table 2: Main hardware components of the 3-DoF spacecraft attitude simulator.

Subsystem	Component	Manufacturer / Model	Description
Platform	Hemispherical air bearing	Physik Instrumente / A-653.045 [22]	Provides nearly frictionless rotational support
	Floating platform	In-house	Supports onboard sensors, actuators, and balancing mechanisms
Sensing	Primary IMU/AHRS	VectorNAV / VN-100 [21]	Provides onboard attitude and angular-rate feedback for control and evaluation
	Secondary IMU	WITmotion / BWT901CL [23]	Used for roll/pitch relative-motion consistency checks
Attitude control	BLDC motor	Maxon / EC-45 flat [24]	Drives each reaction wheel disk
	Motor driver	Maxon / EPOS Compact 50/5 [25]	Commands reaction wheel motor speed
	Motor encoder	Maxon / ENC MILE [26]	Provides wheel speed feedback for motor control
	Wheel disk	In-house	Provides rotational inertia for momentum exchange
Mass balancing	Stepper motor and encoder	Leadshine iCS-RS1706 [27]	Drives the sliding mass mechanism
	Sliding mass	In-house	Adjusts CR-CG offset along each balancing axis
Processing	Control computer	Raspberry Pi / 5	Executes RAMBO, attitude control, and data logging

The distributed onboard components, reaction wheel assemblies, wiring, and sliding masses produce a residual CR-CG offset that can vary with component replacement, cable routing, and platform initialization. Because manual rebalancing is time-consuming and sensitive to such hardware changes, the automatic mass balancing procedure described in Section 3 is employed.

2.2. Mass Balancing Mechanism and Coordinate Frames

The automatic mass balancing subsystem adjusts the platform CG by translating three independently actuated sliding masses. The inertial and body-fixed frames are denoted by $\mathcal{F}_N$ and $\mathcal{F}_B$, respectively, with the origin of $\mathcal{F}_B$ located at the center of rotation (CR) of the air bearing. Unless otherwise stated, all position vectors associated with the mass balancing mechanism are expressed in $\mathcal{F}_B$. Figure 3 shows the coordinate-frame and sliding-mass geometry definitions, while Figure 4 shows the implemented three-axis sliding-mass mechanism.

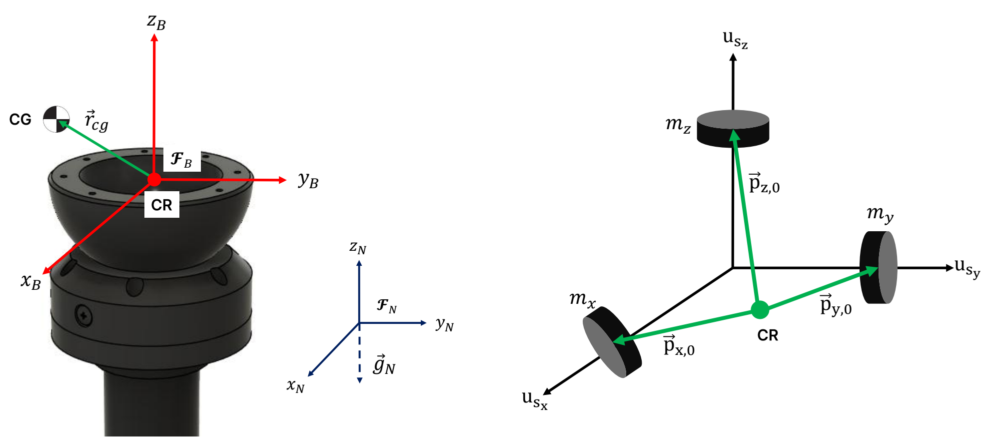

(a) (b)

Figure 3: Coordinate-frame and sliding-mass geometry definitions of the mass balancing system: (**a**) definition of the body-fixed frame $\mathcal{F}_B$, inertial frame $\mathcal{F}_N$, CR-CG offset vector, and gravity vector; (**b**) schematic definition of the sliding-mass reference positions and sliding-axis unit directions.

The CR-CG offset vector is defined as

$$\mathbf{r}_{cg} = \begin{bmatrix} x_{cg} & y_{cg} & z_{cg} \end{bmatrix}^T, \tag{1}$$

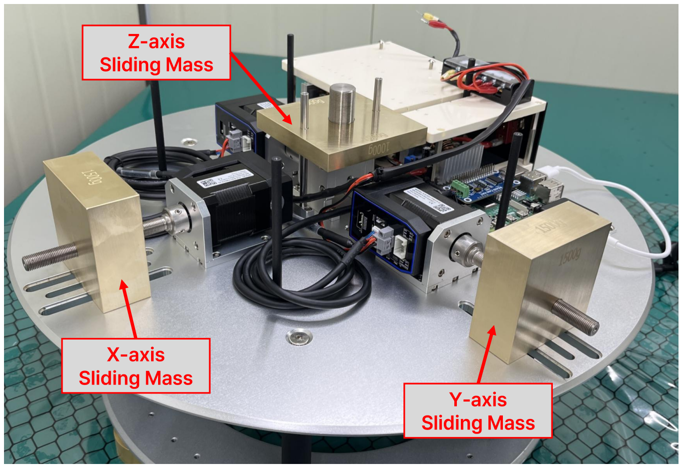

Figure 4: Implemented mass balancing mechanism with three-axis sliding masses.

and the commanded slider-stroke vector is defined as

$$\mathbf{s} = \begin{bmatrix} s_x & s_y & s_z \end{bmatrix}^T, \tag{2}$$

where $\mathbf{r}_{cg}$ is the CG position relative to the CR, and s_i is the commanded displacement of the i-th sliding mass from its reference position. Let m_0 and $\mathbf{r}_0$ denote the equivalent mass and CG position of the platform excluding the sliding masses. The center position of the i-th sliding mass is modeled as

$$\mathbf{p}_i(s_i) = \mathbf{p}_{i,0} + s_i \hat{\mathbf{u}}_{s_i}, \qquad i \in \{x, y, z\}, \tag{3}$$

where $\mathbf{p}_{i,0}$ is its reference position and $\hat{\mathbf{u}}_{s_i}$ is the corresponding sliding-axis unit vector expressed in $\mathcal{F}_B$. The resulting CR-CG offset is

$$\mathbf{r}_{cg}(\mathbf{s}) = \frac{m_0 \mathbf{r}_0 + \sum_{i \in \{x,y,z\}} m_i \mathbf{p}_i(s_i)}{m_{\text{tot}}}, \tag{4}$$

where m_i and m_{tot} denote the individual sliding masses and the total floating mass, respectively. For an incremental slider displacement, the corresponding CR-CG shift is

$$\Delta \mathbf{r}_{cg} = \frac{1}{m_{\text{tot}}} \mathbf{U}_s \mathbf{M}_s \Delta \mathbf{s}, \tag{5}$$

where

$$\mathbf{U}_s = \begin{bmatrix} \hat{\mathbf{u}}_{s_x} & \hat{\mathbf{u}}_{s_y} & \hat{\mathbf{u}}_{s_z} \end{bmatrix}, \qquad \mathbf{M}_s = \mathrm{diag}(m_x, m_y, m_z). \tag{6}$$

Ideally, the sliding axes are aligned with the body-fixed axes, such that $\mathbf{U}_s = \mathbf{I}$. In the actual hardware, slight non-orthogonality caused by assembly and installation errors allows a single-slider displacement to affect multiple components of $\mathbf{r}_{cg}$. This cross-axis coupling motivates the two-stage balancing procedure introduced in Section 3.

2.3. CR-CG Offset and Gravity Disturbance Torque

In a 1-g environment, the residual CR-CG offset generates the following gravity disturbance torque expressed in $\mathcal{F}_B$:

$$\boldsymbol{\tau}_g = \mathbf{r}_{cg}{}^{\times} \left(m_{\mathrm{tot}} \mathbf{g}_B \right), \tag{7}$$

where m_{tot} is the total floating mass of the simulator, $\mathbf{g}_B$ is the gravity vector expressed in $\mathcal{F}_B$, and $\mathbf{r}_{cg}{}^{\times}$ denotes the skew-symmetric matrix of $\mathbf{r}_{cg}$, defined as

$$\mathbf{r}_{cg}{}^{\times} = \begin{bmatrix} 0 & -z_{cg} & y_{cg} \\ z_{cg} & 0 & -x_{cg} \\ -y_{cg} & x_{cg} & 0 \end{bmatrix}. \tag{8}$$

The body-frame gravity vector is obtained from

$$\mathbf{g}_B = \mathbf{C}_{BN} \mathbf{g}_N, \qquad \mathbf{g}_N = \begin{bmatrix} 0 & 0 & -g \end{bmatrix}^T, \tag{9}$$

where $\mathbf{C}_{BN}$ transforms vectors from $\mathcal{F}_N$ to $\mathcal{F}_B$, and g is the gravitational acceleration. When $\mathbf{r}_{cg} = \mathbf{0}$, the gravity disturbance torque vanishes. In practice, however, a small residual offset remains because of sensing uncertainty, actuator resolution, and mechanical assembly errors. Moreover, a hemispherical air-bearing platform becomes statically unstable when the CG is located above the CR, whereas a slightly lower CG provides pendulum-like restoring stability [11]; therefore, the balancing objective is to minimize the residual offset while maintaining $z_{cg} < 0$. Because $\mathbf{g}_B$ varies with platform attitude, the remaining CR-CG offset produces an attitude-dependent gravity torque. In the subsequent hardware attitude-control experiment, the final FRAMBO estimate is used to construct the corresponding model-based feedforward term, as described in Section 4.

2.4. Rigid-Body Rotational Dynamics with Mass Imbalance

The floating platform is modeled as a rigid body rotating about the CR of the hemispherical air bearing. Let $\boldsymbol{\omega} = [\omega_x \ \omega_y \ \omega_z]^T$ denote the angular velocity of $\mathcal{F}_B$ relative to $\mathcal{F}_N$, expressed in $\mathcal{F}_B$. The inertia matrix is

$$\mathbf{J} = \begin{bmatrix} J_{xx} & J_{xy} & J_{xz} \\ J_{yx} & J_{yy} & J_{yz} \\ J_{zx} & J_{zy} & J_{zz} \end{bmatrix}. \tag{10}$$

The inertia properties were estimated from the 3D CAD model of the simulator assembly. Table 1 lists the principal moments of inertia, while the full inertia matrix was used in the attitude-control implementation. Including the residual gravity disturbance torque, the rotational dynamics are

$$\mathbf{J}\dot{\boldsymbol{\omega}} + \boldsymbol{\omega}^{\times}\mathbf{J}\boldsymbol{\omega} = \boldsymbol{\tau}_c + \boldsymbol{\tau}_g + \boldsymbol{\tau}_d, \tag{11}$$

where $\boldsymbol{\tau}_c$ is the reaction-wheel control torque, $\boldsymbol{\tau}_g$ is the gravity disturbance torque defined in Section 2.3, and $\boldsymbol{\tau}_d$ represents unmodeled disturbances, including bearing friction, cable effects, actuator imperfections, and measurement uncertainty. The skew-symmetric angular-velocity matrix is

$$\boldsymbol{\omega}^{\times} = \begin{bmatrix} 0 & -\omega_z & \omega_y \\ \omega_z & 0 & -\omega_x \\ -\omega_y & \omega_x & 0 \end{bmatrix}. \tag{12}$$

For controller design, the angular acceleration is expressed as

$$\dot{\boldsymbol{\omega}} = \mathbf{J}^{-1}\left(\boldsymbol{\tau}_c + \boldsymbol{\tau}_g + \boldsymbol{\tau}_d - \boldsymbol{\omega}^{\times}\mathbf{J}\boldsymbol{\omega}\right). \tag{13}$$

3. Two-Stage Automatic Mass Balancing System

3.1. Overview of RAMBO

The Robust Automatic Mass Balancing Operator (RAMBO) is a pre-test/intermittent mass-balancing framework that reduces the residual CR-CG offset before attitude-control experiments, rather than continuously re-distributing mass during closed-loop control. It combines free-response data processing, batch least-squares offset estimation, slider-command decision logic, and sequential coarse-to-fine operation through CRAMBO and FRAMBO. The overall architecture is shown in Figure 5.

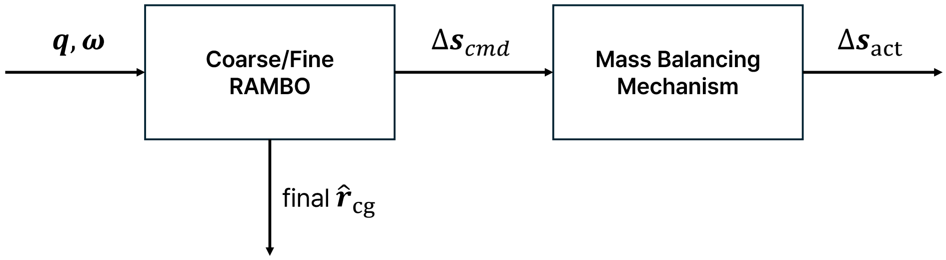

Figure 5: Overall architecture of the Robust Automatic Mass Balancing Operator (RAMBO).

During each balancing execution, the free-response attitude quaternion, $\mathbf{q}$, and angular velocity, $\boldsymbol{\omega}$, are processed to estimate the residual CR-CG offset, $\hat{\mathbf{r}}_{cg}$. The estimate is evaluated against the stage-specific admissible conditions; if further correction is required, RAMBO generates the slider command, $\Delta\mathbf{s}_{cmd}$, with the resulting actual displacement denoted by $\Delta\mathbf{s}_{act}$.

CRAMBO first reduces the initial offset through an automatic iterative loop. After the coarse admissible conditions are satisfied, FRAMBO applies smaller corrections using stop-and-restart operation with platform reinitialization between trials. The final FRAMBO estimate is retained as a model parameter for the subsequent hardware attitude-control experiment, where it is used to construct an attitude-dependent gravity-torque feedforward term as described in Section 4. The batch least-squares estimation procedure is described next.

3.2. Batch Least-Squares-Based CR-CG Offset Estimation

The CR-CG offset is estimated from free-response data using an integrated least-squares approach based on [2, 12]. During each estimation window, the reaction wheel control torque is disabled, and the measured attitude quaternion and angular velocity are used for estimation. A simplified low-rate model is adopted in which gravity torque is treated as the dominant excitation, while products of inertia, gyroscopic coupling, and residual disturbance torques are absorbed into the estimation residual:

$$\dot{\boldsymbol{\omega}} = \begin{bmatrix} \frac{m_{\text{tot}}g}{J_{xx}} \left(-y_{cg}\cos\phi\cos\theta + z_{cg}\sin\phi\cos\theta\right) \\ \frac{m_{\text{tot}}g}{J_{yy}} \left(x_{cg}\cos\phi\cos\theta + z_{cg}\sin\theta\right) \\ \frac{m_{\text{tot}}g}{J_{zz}} \left(-x_{cg}\sin\phi\cos\theta - y_{cg}\sin\theta\right) \end{bmatrix}, \tag{14}$$

where ϕ and θ are the roll and pitch angles reconstructed from the attitude quaternion. This simplified model is used only for RAMBO offset estimation; the full inertia matrix is retained in the attitude-control implementation.

Integration over the sampling interval $[t_k, t_{k+1}]$ yields

$$\Delta\boldsymbol{\omega}_k = \boldsymbol{\Phi}_k \mathbf{r}_{cg}, \tag{15}$$

where

$$\Delta\boldsymbol{\omega}_k = \begin{bmatrix} \omega_{x,k+1} - \omega_{x,k} \\ \omega_{y,k+1} - \omega_{y,k} \\ \omega_{z,k+1} - \omega_{z,k} \end{bmatrix}, \qquad \mathbf{r}_{cg} = \begin{bmatrix} x_{cg} & y_{cg} & z_{cg} \end{bmatrix}^T. \tag{16}$$

Using trapezoidal integration, the regression matrix is

$$\boldsymbol{\Phi}_k = \begin{bmatrix} 0 & \Phi_{12,k} & \Phi_{13,k} \\ \Phi_{21,k} & 0 & \Phi_{23,k} \\ \Phi_{31,k} & \Phi_{32,k} & 0 \end{bmatrix}, \tag{17}$$

with

$$\Phi_{12,k} = -\frac{m_{\text{tot}}g\Delta t}{2J_{xx}} \left[(\cos\phi\cos\theta)_{k+1} + (\cos\phi\cos\theta)_k\right], \tag{18}$$

$$\Phi_{13,k} = \frac{m_{\text{tot}}g\Delta t}{2J_{xx}} \left[(\sin\phi\cos\theta)_{k+1} + (\sin\phi\cos\theta)_k\right], \tag{19}$$

$$\Phi_{21,k} = \frac{m_{\text{tot}}g\Delta t}{2J_{yy}} \left[(\cos\phi\cos\theta)_{k+1} + (\cos\phi\cos\theta)_k\right], \tag{20}$$

$$\Phi_{23,k} = \frac{m_{\text{tot}}g\Delta t}{2J_{yy}} \left[(\sin\theta)_{k+1} + (\sin\theta)_k\right], \tag{21}$$

$$\Phi_{31,k} = -\frac{m_{\text{tot}}g\Delta t}{2J_{zz}} \left[(\sin\phi\cos\theta)_{k+1} + (\sin\phi\cos\theta)_k\right], \tag{22}$$

$$\Phi_{32,k} = -\frac{m_{\text{tot}}g\Delta t}{2J_{zz}} \left[(\sin\theta)_{k+1} + (\sin\theta)_k\right], \tag{23}$$

where $\Delta t = t_{k+1} - t_k$ is the sampling interval. Stacking the N sampling intervals yields

$$\Delta\boldsymbol{\Omega}_L = \boldsymbol{\Phi}_L \mathbf{r}_{cg}, \tag{24}$$

where

$$\Delta\boldsymbol{\Omega}_L = \begin{bmatrix} \Delta\boldsymbol{\omega}_1 \\ \Delta\boldsymbol{\omega}_2 \\ \vdots \\ \Delta\boldsymbol{\omega}_N \end{bmatrix}, \qquad \boldsymbol{\Phi}_L = \begin{bmatrix} \boldsymbol{\Phi}_1 \\ \boldsymbol{\Phi}_2 \\ \vdots \\ \boldsymbol{\Phi}_N \end{bmatrix}. \tag{25}$$

Assuming that $\boldsymbol{\Phi}_L$ has full column rank, the batch least-squares estimate is

$$\hat{\mathbf{r}}_{cg} = \left(\boldsymbol{\Phi}_L^T \boldsymbol{\Phi}_L\right)^{-1} \boldsymbol{\Phi}_L^T \Delta\boldsymbol{\Omega}_L. \tag{26}$$

The estimate $\hat{\mathbf{r}}_{cg}$ is interpreted as a dynamic-equivalent CR-CG offset estimate rather than an independent measurement of the physical CR-CG offset. It is the model-consistent parameter that best explains the measured free-response motion and may absorb sensor noise, bias drift, unmodeled disturbance torques, and modeling approximations. In this study, the estimate is used first for slider correction and subsequently as a model parameter for constructing an attitude-dependent gravity-torque feedforward term in the hardware attitude-control experiment. Figure 6 summarizes the estimation and decision logic used in RAMBO.

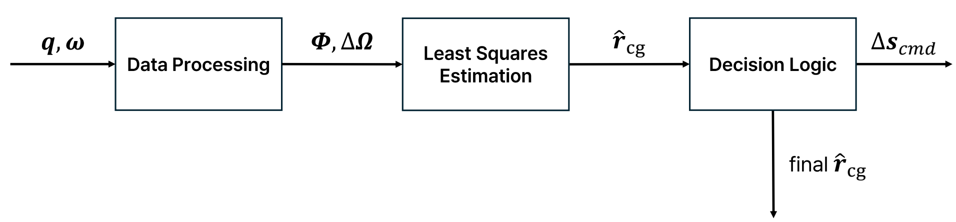

Figure 6: Batch least-squares CR-CG offset estimation and decision logic in RAMBO.

Using a nominal diagonal mass-shift relation, the raw slider correction is computed as

$$\Delta s_{\mathrm{raw},i} = (\hat{r}_{cg,\mathrm{tar},i} - \hat{r}_{cg,i}) \frac{m_{\mathrm{tot}}}{m_i}, \qquad i \in \{x, y, z\}. \tag{27}$$

The full non-orthogonal slider-axis matrix, $\mathbf{U}_s$, is not explicitly identified. Instead, residual cross-axis coupling and command errors are addressed through repeated estimate-and-correct operation and stage-dependent weighting. The final command, $\Delta\mathbf{s}_{\mathrm{cmd}}$, is determined by the CRAMBO or FRAMBO decision logic described in Sections 3.3 and 3.4, respectively.

3.3. Coarse Balancing Stage: CRAMBO

Coarse RAMBO (CRAMBO) is the first-stage automatic iterative procedure that reduces the initial CR-CG offset to a coarse admissible range before FRAMBO. At each iteration, attitude and angular-velocity data are collected during a free-response window of duration $t_{\mathrm{C,win}}$ and processed using the batch least-squares method in Section 3.2 to obtain $\hat{\mathbf{r}}_{cg}$. The estimate is then evaluated against the coarse lateral condition

$$|\hat{x}_{cg}| \leq \alpha_C \quad \text{and} \quad |\hat{y}_{cg}| \leq \alpha_C, \tag{28}$$

and the vertical admissible range

$$\beta_{C,l} \leq \hat{z}_{cg} \leq \beta_{C,u}, \tag{29}$$

where α_C is the allowable lateral bound, and $\beta_{C,l}$ and $\beta_{C,u}$ are the lower and upper vertical bounds, respectively. The vertical range is defined below the CR to retain pendulum-like restoring stability.

If either admissible condition is not satisfied, the raw slider corrections are converted into CRAMBO commands using stage-dependent weighting. The lateral commands may be scaled by $w_{C,\alpha}$ according to the vertical-offset condition, while the vertical command is scaled by $w_{C,\beta,k}$ according to the corresponding vertical-offset region. These weighting factors provide conservative corrections under cross-axis coupling and actuator repeatability errors.

CRAMBO repeats the estimate-and-correct procedure until both the lateral and vertical admissible conditions are satisfied. The resulting coarse-balanced condition provides a stable initial state for the subsequent FRAMBO stage rather than the final balancing accuracy. Figure 7 summarizes the CRAMBO operation.

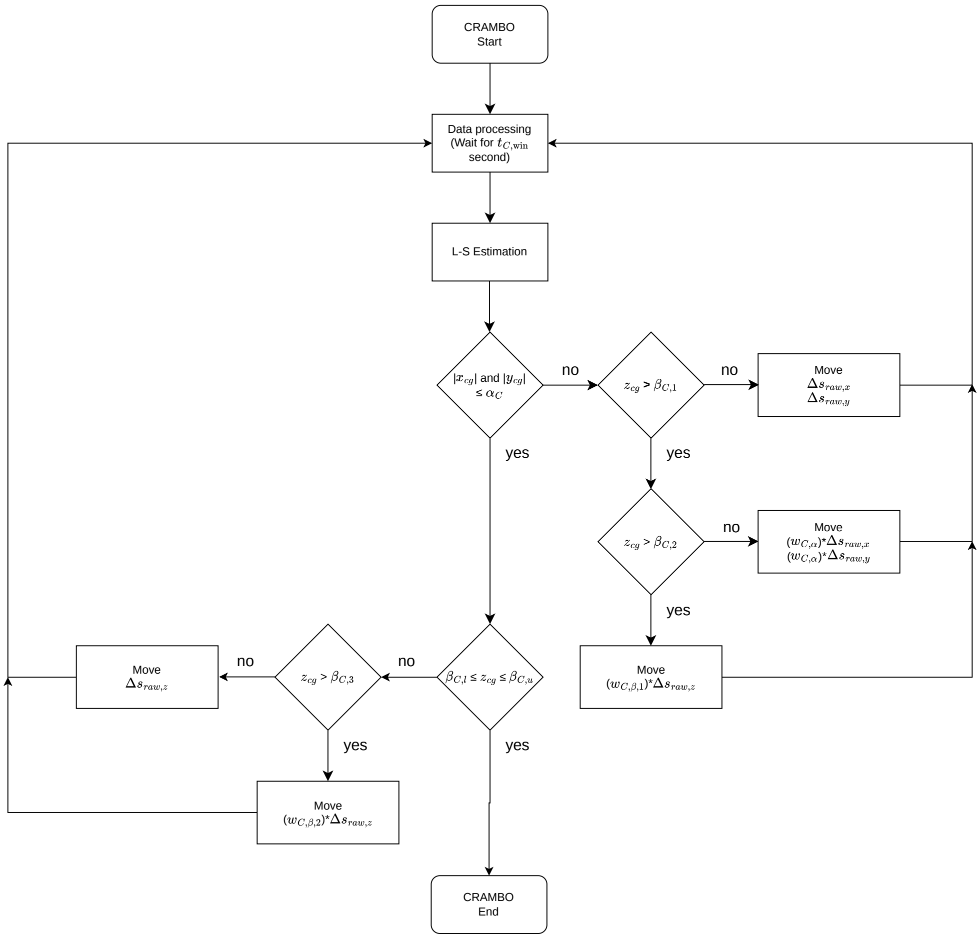

Figure 7: Operational flowchart of the Coarse RAMBO (CRAMBO) stage.

3.4. Fine Balancing Stage: FRAMBO

Fine RAMBO (FRAMBO) is the second-stage procedure that refines the residual CR-CG offset after CRAMBO. Unlike the automatic iterative CRAMBO loop, each FRAMBO trial performs one free-response estimation and, if required, one slider correction. The platform is then stopped and reinitialized before the next trial to reduce the influence of transient motion and residual oscillation on the subsequent estimate.

During each trial, attitude and angular-velocity data are collected over the estimation window, $t_{\mathrm{F,win}}$, and processed using the batch least-squares method in Section 3.2 to obtain $\hat{\mathbf{r}}_{cg}$. The estimate is evaluated against the fine lateral condition

$$|\hat{x}_{cg}| \leq \alpha_F \quad \text{and} \quad |\hat{y}_{cg}| \leq \alpha_F, \tag{30}$$

and the fine vertical admissible range

$$\beta_{F,l} \leq \hat{z}_{cg} \leq \beta_{F,u}, \tag{31}$$

where α_F is the allowable lateral bound, and $\beta_{F,l}$ and $\beta_{F,u}$ are the lower and upper vertical bounds, respectively. The vertical range remains below the CR to preserve passive pendulum-like stability while reducing the residual gravity torque.

If either admissible condition is not satisfied, FRAMBO converts the raw slider corrections into smaller, condition-dependent commands. The intermediate vertical thresholds, $\beta_{F,1}$ through $\beta_{F,5}$, determine whether lateral, vertical, or weighted correction is applied, while $w_{F,\alpha}$ and $w_{F,\beta,1}, \ldots, w_{F,\beta,4}$ limit the corresponding correction magnitude. This conservative command strategy reduces overcorrection and residual cross-axis coupling near the fine admissible range.

Each FRAMBO execution terminates after one slider command is applied, and successive trials are performed using the stop-and-restart procedure described above. FRAMBO is completed when both the lateral and vertical admissible conditions are satisfied. The final estimate, $\hat{\mathbf{r}}_{cg}$, represents the dynamic-equivalent CR-CG offset estimate for the final balanced configuration and is retained as a fixed model parameter during the subsequent hardware attitude-control maneuver, where it is used to construct an attitude-dependent gravity-torque feedforward term. Figure 8 summarizes the FRAMBO operation.

3.5. Summary of RAMBO Operational Logic

Table 3 compares the operational roles of CRAMBO and FRAMBO. Both stages use the batch least-squares estimator described in Section 3.2; CRAMBO performs rapid coarse correction through an automatic iterative loop, whereas FRAMBO applies conservative single-step corrections with platform stop-and-restart operation.

The final FRAMBO estimate, $\hat{\mathbf{r}}_{cg}$, is retained as a fixed model parameter for the subsequent hardware attitude-control maneuver, as described in Section 4.

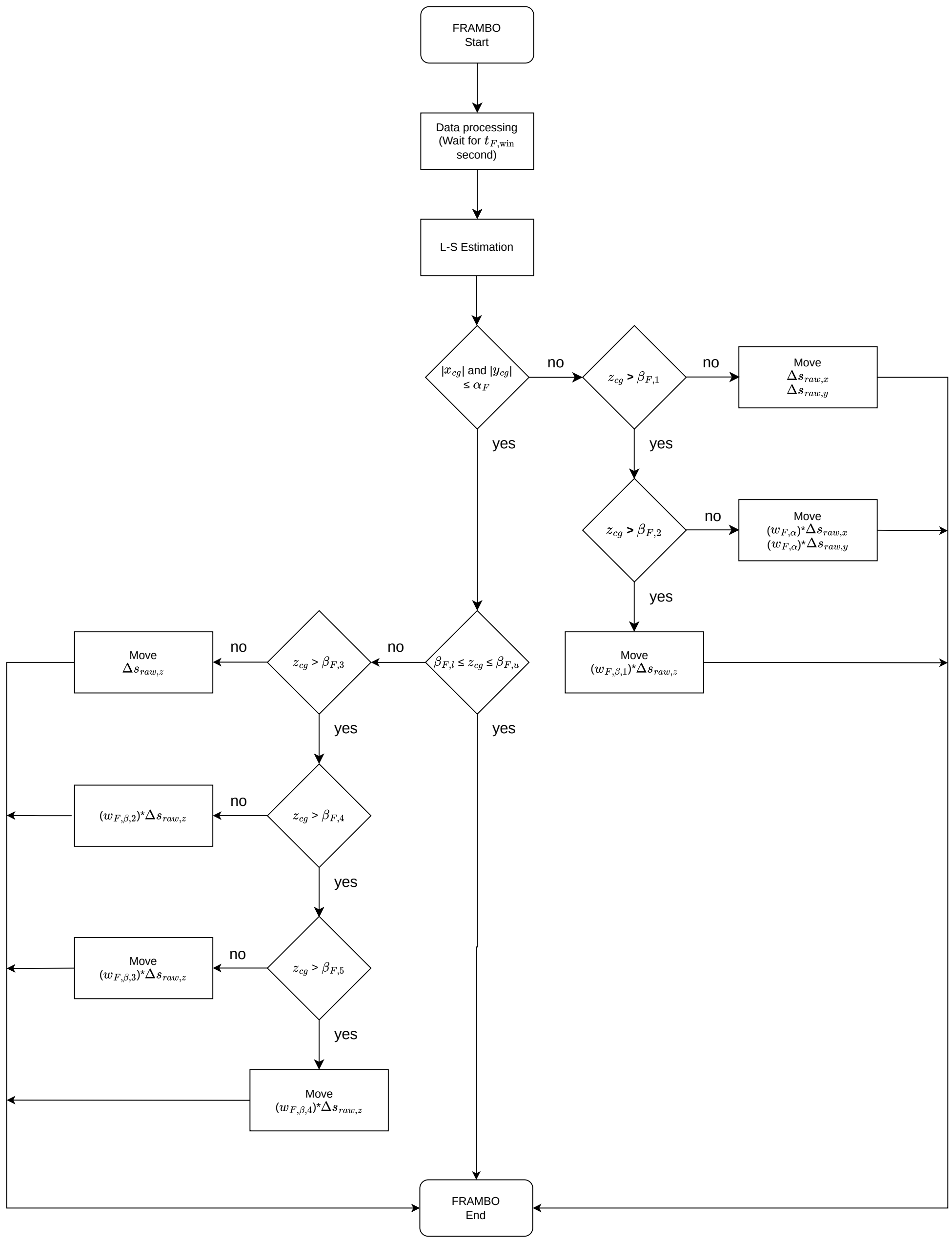

Figure 8: Operational flowchart of the Fine RAMBO (FRAMBO) stage.

Table 3: Key operational differences between CRAMBO and FRAMBO.

Item	**CRAMBO**	**FRAMBO**
Purpose	Rapid coarse reduction of the initial CR-CG offset	Fine refinement of the residual CR-CG offset
Execution mode	Automatic iterative loop	Single-step execution with platform stop-and-restart operation
Correction strategy	Relatively large correction using coarse bounds	Reduced and condition-dependent correction to avoid overcorrection
Final role	Provides a coarse admissible initial condition for FRAMBO	Provides the final offset estimate retained for subsequent hardware attitude control

4. Attitude Control Implementation

A small residual CR-CG offset remains after RAMBO because of hardware resolution, sensing uncertainty, and the negative vertical-offset requirement for platform stability. For the subsequent hardware attitude-control experiment, the final FRAMBO estimate, $\hat{\mathbf{r}}_{cg}$, is retained as a fixed model parameter and used to construct an attitude-dependent gravity-torque feedforward term within a conventional quaternion PD controller. The feedforward term represents the estimated offset-induced torque, while the PD feedback provides closed-loop stabilization under residual modeling errors and unmodeled disturbances.

4.1. Quaternion PD Control with Gravity-Torque Feedforward

Following the conventional quaternion feedback formulation [19, 20], the current and target attitudes are represented using scalar-last unit quaternions as

$$\mathbf{q}_s = \begin{bmatrix} \mathbf{q}_{s,v}^T & q_{s,4} \end{bmatrix}^T, \qquad \mathbf{q}_t = \begin{bmatrix} \mathbf{q}_{t,v}^T & q_{t,4} \end{bmatrix}^T, \tag{32}$$

where the subscripts s and t denote the current and target attitudes, respectively, and $\mathbf{q}_{j,v}$ and $q_{j,4}$ are the vector and scalar parts for $j \in \{s, t\}$. The attitude error quaternion is defined as

$$\mathbf{q}_e = (\mathbf{q}_t^{-1})^{\otimes} \mathbf{q}_s = \begin{bmatrix} \mathbf{q}_{e,v}^T & q_{e,4} \end{bmatrix}^T, \tag{33}$$

where $(\cdot)^{\otimes}$ denotes the quaternion multiplication matrix operator. To resolve the sign ambiguity arising from the double-covering property, the sign of $\mathbf{q}_e$ is selected such that $q_{e,4} \geq 0$.

The angular-velocity error is defined as

$$\boldsymbol{\omega}_e = \boldsymbol{\omega}_c - \boldsymbol{\omega}, \tag{34}$$

where $\boldsymbol{\omega}_c$ and $\boldsymbol{\omega}$ are the commanded and measured angular velocities expressed in $\mathcal{F}_B$, respectively. The quaternion PD torque is

$$\boldsymbol{\tau}_{PD} = -\mathbf{K}_p \mathbf{q}_{e,v} - \mathbf{K}_d \boldsymbol{\omega}_e, \tag{35}$$

where $\mathbf{K}_p$ and $\mathbf{K}_d$ are the proportional and derivative gain matrices, respectively. For the fixed target attitude used in this study, $\boldsymbol{\omega}_c = \mathbf{0}$. Residual gravity torque caused by the CR-CG offset can degrade the pointing accuracy of air-bearing simulators [28]. The final FRAMBO estimate, $\hat{\mathbf{r}}_{cg}$, is used to evaluate the gravity-torque component predicted by the model in Section 2.3:

$$\hat{\boldsymbol{\tau}}_g = \hat{\mathbf{r}}_{cg}{}^{\times} \left(m_{\text{tot}} \mathbf{g}_B \right). \tag{36}$$

The commanded platform torque combines the quaternion PD torque with a model-based feedforward term defined as the negative of the estimated gravity torque:

$$\boldsymbol{\tau}_c = \boldsymbol{\tau}_{PD} - \hat{\boldsymbol{\tau}}_g. \tag{37}$$

During the attitude-control experiment, $\hat{\mathbf{r}}_{cg}$ is held fixed, whereas $\mathbf{g}_B$ is updated from the measured attitude. The resulting feedforward term therefore varies with attitude and opposes the gravity-torque component predicted by the adopted model. Exact cancellation is not assumed because estimation errors, modeling approximations, and unmodeled disturbances may remain; quaternion PD feedback provides closed-loop stabilization under these residual effects.

4.2. Reaction Wheel Torque Command Generation

The three reaction wheels are aligned with the body-fixed axes; therefore, no redundant control allocation is required. Because the rotor torque produces an equal and opposite reaction torque on the platform, the commanded wheel-torque vector is

$$\boldsymbol{\tau}_{rw,cmd} = \begin{bmatrix} \tau_{rw,x,cmd} & \tau_{rw,y,cmd} & \tau_{rw,z,cmd} \end{bmatrix}^T = -\boldsymbol{\tau}_c. \tag{38}$$

For the i-th reaction wheel, the rotor torque is related to the wheel acceleration by

$$\tau_{rw,i} = J_{rw}\dot{\Omega}_i, \qquad i \in \{x, y, z\}, \tag{39}$$

where J_{rw} and Ω_i are the wheel inertia and angular speed, respectively. With the discrete command-update interval Δt, the wheel-speed command is updated as

$$\Omega_{i,cmd}(k+1) = \Omega_{i,cmd}(k) + \frac{\tau_{rw,i,cmd}}{J_{rw}}\Delta t. \tag{40}$$

The torque and wheel-speed commands are constrained by the operational limits summarized in Table 1. Figure 9 shows the orthogonal three-axis reaction wheel configuration.

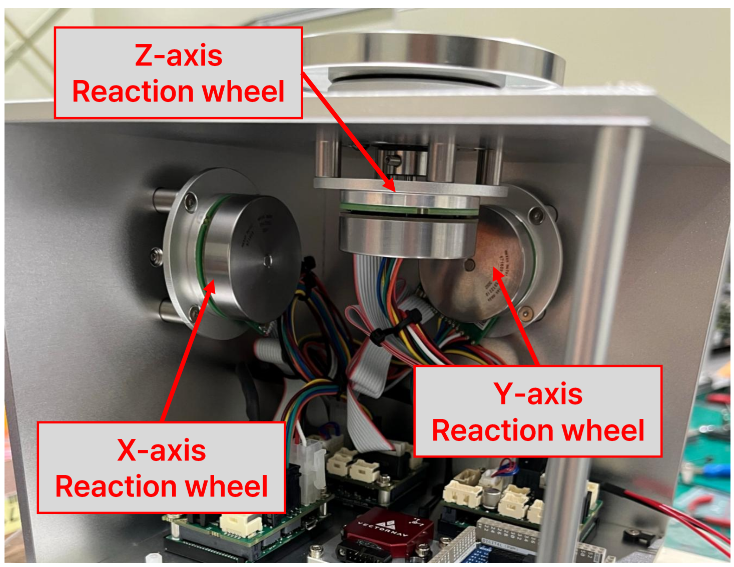

Figure 9: Three-axis orthogonal reaction wheel configuration used for attitude control torque generation.

5. Validation Results

5.1. Experimental Setup

Hardware validation comprised RAMBO-based mass balancing followed by attitude-control testing using the final balanced configuration. The CRAMBO and FRAMBO admissible conditions and decision-logic parameters are summarized in Table 4.

Table 4: RAMBO admissible conditions and decision-logic parameters.

Category	Parameter	Value	Unit
Requirement	CRAMBO lateral admissible condition	$\lvert\hat{x}_{cg}\rvert,\ \lvert\hat{y}_{cg}\rvert < 1$	µm
	CRAMBO vertical admissible range	$-100 < \hat{z}_{cg} < -70$	µm
	FRAMBO lateral admissible condition	$\lvert\hat{x}_{cg}\rvert,\ \lvert\hat{y}_{cg}\rvert < 0.5$	µm
	FRAMBO vertical admissible range	$-30 < \hat{z}_{cg} < -20$	µm
Control	IMU sampling rate	50	Hz
CRAMBO	Target vertical offset, $\hat{z}_{cg,tar}$	-75	µm
	Estimation window, $t_{C,\mathrm{win}}$	40	sec
	Intermediate vertical bounds, $\beta_{C,k}$	$-100,\ -70,\ -100$	µm
	Lateral weighting factor, $w_{C,\alpha}$	0.5	–
	Vertical weighting factors, $w_{C,\beta,k}$	$0.6,\ 0.6$	–
FRAMBO	Target vertical offset, $\hat{z}_{cg,tar}$	-25	µm
	Estimation window, $t_{F,\mathrm{win}}$	80	sec
	Intermediate vertical bounds, $\beta_{F,k}$	$-100,\ -20,\ -100,\ -50,\ -20$	µm
	Lateral weighting factor, $w_{F,\alpha}$	0.5	–
	Vertical weighting factors, $w_{F,\beta,k}$	$0.3,\ 0.6,\ 0.3,\ 0.3$	–

These parameters define the balancing requirements, target vertical offsets, estimation windows, and weighting factors used in the mass balancing experiment. Using the final balanced configuration, a coupled three-axis maneuver from $(0°, 0°, 0°)$ to $(15°, -10°, 35°)$ was conducted using the conventional quaternion PD controller with the FRAMBO-estimate-based gravity-torque feedforward term applied. The final FRAMBO estimate was held fixed throughout the maneuver. Table 5 summarizes the attitude-control requirements, controller gains, and test conditions. Performance was evaluated using the attitude and angular-velocity tracking errors and the commanded and measured reaction wheel speeds.

Although the RW command/encoder communication was performed at 5 Hz, the wheel-speed command value was updated every 1.0 s and held constant between updates. This command update interval was selected to allow the reaction wheel speed response to settle sufficiently before the next command update, as illustrated in Fig. 10.

Table 5: Attitude-control test conditions and controller parameters.

Category	**Parameter**	**Value**	**Unit**
Requirement	Attitude error	< 1	deg
	Angular velocity error	< 0.5	deg/s
Control	IMU sampling rate	50	Hz
	RW command/encoder communication rate	5	Hz
	RW speed command update interval	1.0	s
	Proportional gain, $\mathbf{K}_p$	diag([0.27, 0.28, 0.10])	N·m
	Derivative gain, $\mathbf{K}_d$	diag([1.00, 1.04, 0.36])	N·m·s
Test case	Initial attitude	$[0,\ 0,\ 0]^T$	deg
	Target attitude	$[15,\ -10,\ 35]^T$	deg
	Target angular velocity	$[0,\ 0,\ 0]^T$	deg/s
Control deadband	Attitude error deadband	0.3	deg
	Angular velocity error deadband	0.3	deg/s

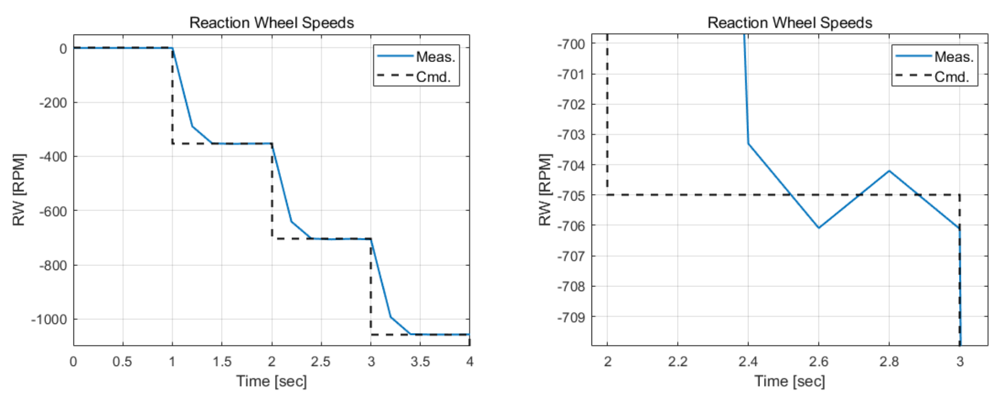

(a) (b)

Figure 10: Reaction wheel speed response used to justify the wheel-speed command update interval: (**a**) overall command and measured speed response; (**b**) enlarged view showing speed settling within one command update interval.

5.2. CRAMBO/FRAMBO Mass Balancing Results

Before CRAMBO, the platform was manually pre-balanced to prevent excessive initial tipping; therefore, the results represent automatic refinement of the remaining residual CR-CG offset. Table 6 summarizes the eight CRAMBO iterations and eleven FRAMBO trials, through which the estimated offset changed from $[1.562,\ 1.810,\ -265.142]^T$ µm to $[0.083,\ 0.115,\ -27.621]^{\mathrm{T}}$ µm.

Table 6: Summary of CR-CG offset convergence before and after each RAMBO stage.

Stage	**Executions**	**Initial $\hat{\mathbf{r}}_{cg}$ [µm]**	**Final $\hat{\mathbf{r}}_{cg}$ [µm]**
CRAMBO	8 iterations	$[1.562,\ 1.810,\ -265.142]^T$	$[0.303,\ 0.005,\ -95.083]^T$
FRAMBO	11 trials	$[0.232,\ 0.393,\ -84.336]^T$	$[0.083,\ 0.115,\ -27.621]^T$

Detailed balancing records are provided in Appendix A. In the final two FRAMBO trials, no additional slider command was applied, and the estimates were $[0.0848,\ 0.0938,\ -23.1258]^T$ µm and $[0.0830,\ 0.1146,\ -27.6205]^T$ µm, respectively. Both remained within the fine admissible range, providing repeatable dynamic-equivalent CR-CG offset estimates for the final balanced configuration.

Figure 11 shows that CRAMBO brought the estimated offset into the coarse admissible range within eight iterations, while maintaining micrometer-level lateral components and a negative vertical offset.

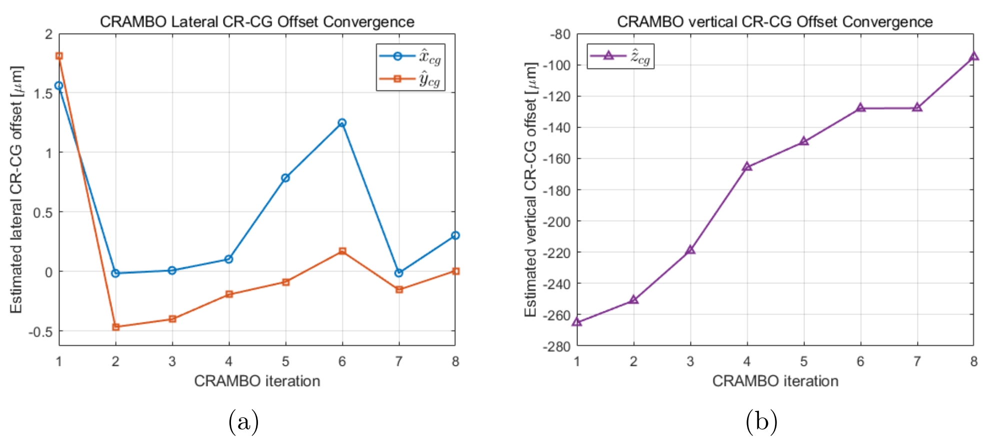

Figure 11: Estimated CR-CG offset convergence during the CRAMBO balancing test: (**a**) lateral components; (**b**) vertical component.

Figure 12 shows that FRAMBO brought the estimated residual CR-CG offset into the fine admissible range over eleven stop-and-restart trials, despite trial-to-trial variations associated with estimation uncertainty and cross-axis coupling.

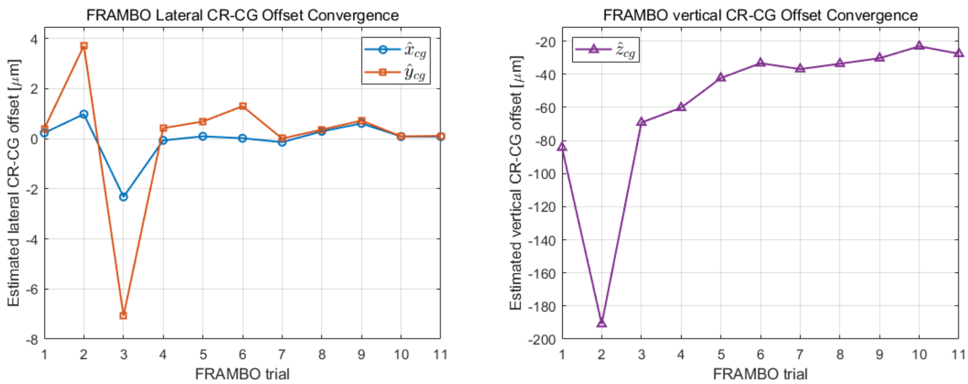

(a) (b)

Figure 12: Estimated CR-CG offset convergence during the FRAMBO balancing test: (**a**) lateral components; (**b**) vertical component.

Figure 13 compares the free-response roll and pitch motions before CRAMBO and after FRAMBO. The post-FRAMBO amplitude is not necessarily smaller because reducing $|z_{cg}|$ weakens the passive pendulum stiffness, while the response amplitude also depends on the release condition. Therefore, the free-response change should be interpreted together with the dominant oscillation period and the estimated CR-CG offset convergence.

For a secondary quantitative interpretation, the mean-removed roll and pitch responses were characterized by their peak amplitudes and dominant periods. Under a small-angle equivalent-pendulum approximation, neglecting damping for the period estimate,

$$J_{\mathrm{eq}}\ddot{\theta} + k_\theta \theta = 0, \qquad k_\theta \approx m_{\mathrm{tot}} g h, \qquad T \approx 2\pi \sqrt{\frac{J_{\mathrm{eq}}}{k_\theta}}, \tag{41}$$

where $h = |z_{cg}|$, J_{eq} is the equivalent roll-pitch inertia, and T is the dominant oscillation period. The relative stiffness and equivalent pendulum-mode energy ratios are estimated as

$$\frac{k_{\theta,a}}{k_{\theta,b}} \approx \left(\frac{T_b}{T_a}\right)^2, \qquad \frac{E_a}{E_b} \approx \left(\frac{\theta_{rp,a}}{\theta_{rp,b}}\right)^2 \left(\frac{T_b}{T_a}\right)^2, \tag{42}$$

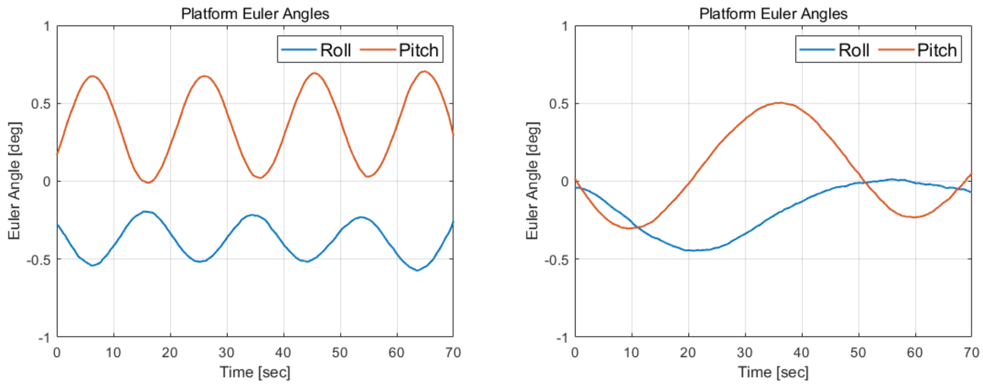

(a) (b)

Figure 13: Free-response roll and pitch responses before and after automatic mass balancing: (**a**) manually pre-balanced condition before CRAMBO; (**b**) final balanced condition after FRAMBO.

where the subscripts b and a denote the conditions before CRAMBO and after FRAMBO, respectively, and $\theta_{rp} = \sqrt{{\theta_{r,\max}}^2 + {\theta_{p,\max}}^2}$ is the root-sum-square peak metric of the roll and pitch responses. As summarized in Table 7, the dominant period increased from approximately 20 to 50 s. Assuming a negligible change in J_{eq}, this corresponds to an effective restoring-stiffness ratio of 0.16. Although the root-sum-square peak metric increased from approximately 0.38° to 0.50°, the corresponding equivalent pendulum-mode energy ratio was estimated as 0.28. This ratio is a model-based indicator of the free-response change rather than a direct measurement of mechanical energy.

Table 7: Free-response roll-pitch oscillation comparison before CRAMBO and after FRAMBO.

Condition	**Roll peak [deg]**	**Pitch peak [deg]**	**Combined peak [deg]**	**Dominant period [s]**	**Stiffness ratio**	**Energy ratio**
Before CRAMBO	0.1901	0.3291	0.3801	20	1.000	1.000
After FRAMBO	0.1894	0.4612	0.4985	50	0.160	0.275

5.3. *Three-Axis Diagonal Maneuver Experiment and Tracking Error Analysis*

Following RAMBO, the hardware testbed executed a coupled three-axis maneuver from $(0°, 0°, 0°)$ to $(15°, -10°, 35°)$. Figure 14 presents the attitude responses and tracking errors measured by the primary VN-100, together with the secondary WITMotion roll/pitch measurements. Based on the VN-100 estimates, the roll, pitch, and yaw tracking errors settled within approximately $\pm 0.5°$. The WITMotion measurements are included only as a relative roll/pitch consistency check after initial-offset removal and sign-convention correction, rather than as an independent ground-truth reference.

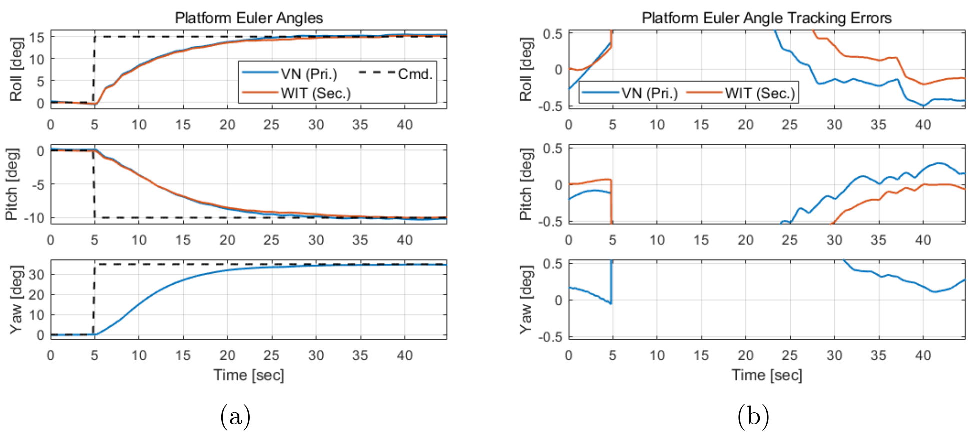

Figure 14: Platform attitude response and tracking errors during the three-axis diagonal maneuver: (**a**) commanded Euler angles and responses measured by the primary VN-100 and secondary WITMotion IMUs; (**b**) corresponding tracking errors. WITMotion measurements are shown only for roll and pitch because its yaw estimate was unreliable in the experimental magnetic environment.

Figure 15 shows the angular velocity response and tracking error during the maneuver. Based on the VN-100 estimates, the steady-state errors remained within approximately $\pm 0.4°/\text{s}$ for roll and $\pm 0.2°/\text{s}$ for pitch and yaw, with bounded residual oscillations.

Figure 16 shows that the measured wheel speeds followed the commanded responses and remained within the allowable operating range. Together with the bounded attitude and angular-velocity errors, these measurements document stable three-axis hardware tracking in the final RAMBO-balanced configuration with the FRAMBO-estimate-based gravity-torque feedforward term applied.

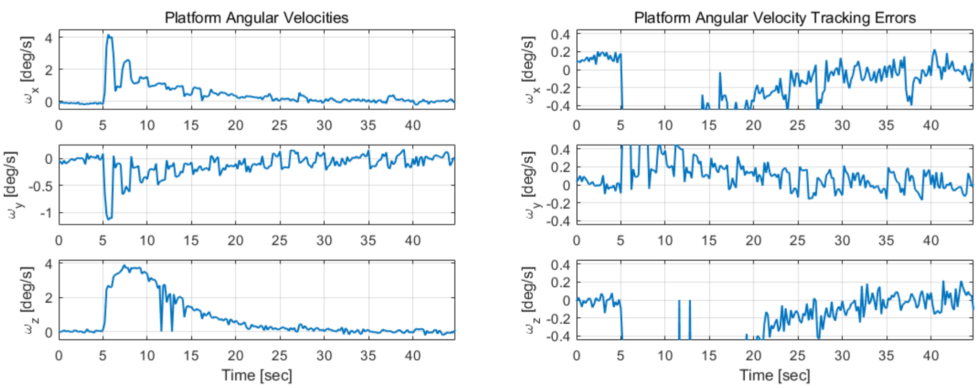

(a) (b)

Figure 15: Platform angular velocity response and angular velocity tracking error during the three-axis diagonal maneuver: (**a**) angular velocity response; (**b**) angular velocity tracking error.

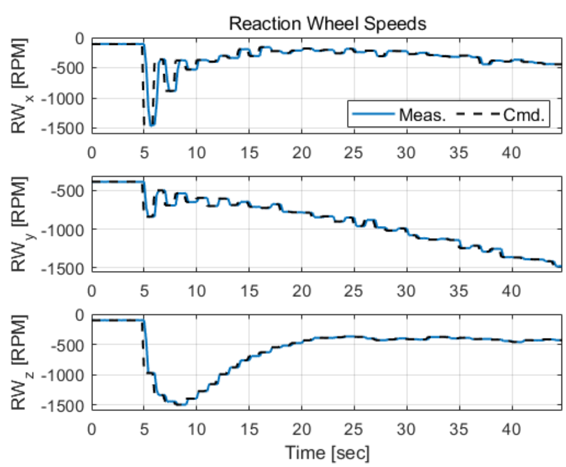

Figure 16: Reaction wheel speed commands and measured wheel speeds during the three-axis diagonal maneuver.

6. Discussion

Perfect CR-CG alignment is not the balancing objective because a slightly negative vertical offset, $z_{cg} < 0$, is intentionally retained to provide passive restoring stability. Accordingly, the final balanced condition reduces the residual gravity disturbance torque subject to this stability constraint. Because the feedforward term is constructed from $\hat{\mathbf{r}}_{cg}$, any discrepancy between the true residual offset and the FRAMBO estimate results in a difference between the gravity torque predicted by the adopted model and the actual disturbance acting on the platform. This sensitivity was not quantified explicitly in the present study. In addition, because a PD-only hardware baseline was not included, the independent performance contribution of the feedforward term could not be isolated or quantified. The reported maneuver therefore demonstrates stable tracking of the implemented PD-plus-feedforward configuration as a whole, rather than the effectiveness of the feedforward term alone.

The full non-orthogonal slider-axis matrix, $\mathbf{U}_s$, was not separately identified. Accordingly, RAMBO should not be interpreted as a geometric calibration or real-time decoupling method; cross-axis effects remain as implementation uncertainties handled through iterative estimate-and-correct operation. The switching thresholds and weighting factors were selected empirically for the present hardware configuration. Therefore, RAMBO does not provide a formal global convergence guarantee for arbitrary initial offsets or slider-axis coupling; convergence was demonstrated only from the tested manually pre-balanced initial condition. The 1.0-s wheel-speed command update interval limits the present implementation to relatively low-bandwidth maneuvers; higher-bandwidth testing will require faster command updating and explicit consideration of the reaction wheel dynamics.

The framework relies on IMU-based attitude and angular-rate measurements for both CR-CG offset estimation and attitude control; therefore, measurement errors can affect the balancing result and closed-loop performance. The reported micrometer-level values are not independent measurements of the physical CR-CG offset because sensor errors and unmodeled mechanical disturbances may be absorbed into the batch least-squares estimate. Accordingly, $\hat{\mathbf{r}}_{cg}$ should be interpreted as a dynamic-equivalent CR-CG offset estimate used within the adopted model for slider correction and, after balancing, for constructing the gravity-torque feedforward term used in the hardware attitude-control experiment. The present implementation is limited to pre-test/intermittent balancing: the final FRAMBO estimate is held fixed during the subsequent attitude-control maneuver, and time-varying changes in the mass distribution are not estimated online. Furthermore, the experiments were conducted within the allowable motion range of the hemispherical air-bearing platform; therefore, the results demonstrate ground-based ADCS validation rather than direct in-orbit performance.

7. Conclusions

This study presented and experimentally validated a two-stage RAMBO framework, comprising CRAMBO and FRAMBO, for automatic CR-CG balancing of a hemispherical 3-DoF spacecraft attitude simulator. CRAMBO provided rapid coarse offset reduction, whereas FRAMBO refined the residual offset through sequential stop-and-restart trials.

The CRAMBO stage was completed after eight iterations, and the FRAMBO stage was completed after eleven trials. The final dynamic-equivalent CR-CG offset estimate converged to approximately $[0.08,\ 0.12,\ -27.62]$ μm, indicating micrometer-level estimated lateral components while retaining the required negative vertical offset. For the subsequent hardware attitude-control experiment, this final estimate was retained as a fixed model parameter and used to construct an attitude-dependent gravity-torque feedforward term within a conventional quaternion PD controller. During the three-axis diagonal maneuver from $(0°, 0°, 0°)$ to $(15°, -10°, 35°)$, the steady-state attitude errors remained within approximately $\pm 0.5°$ based on the onboard VN-100 estimates, with the roll and pitch responses additionally checked using a secondary IMU. The corresponding angular velocity errors remained within approximately $\pm 0.4°$/s for roll and $\pm 0.2°$/s for pitch and yaw. These results demonstrate the hardware implementation of the two-stage RAMBO procedure and the subsequent use of its final estimate in three-axis attitude-control testing. The experiment did not isolate the performance contribution of the feedforward term or demonstrate exact cancellation of the residual gravity torque.

Future work will focus on three areas: vision-based external ground-truth measurements for independent evaluation of the attitude response and dynamic-equivalent CR-CG offset estimate; hardware calibration of the sliding-mass geometry and reaction wheel characteristics; and higher-bandwidth implementation through faster wheel-command updates and explicit modeling of the actuator dynamics.

Appendix A. Detailed RAMBO Balancing Results

Tables A.1 and A.2 summarize the detailed CRAMBO and FRAMBO balancing records. Here, $\Delta s_{\text{raw},i}$ denotes the correction value computed before decision weighting, $\Delta s_{\text{cmd},i}$ denotes the applied slider command after the RAMBO decision logic, and enc_i denotes the accumulated encoder position.

Table A.1: Detailed CRAMBO balancing records. The estimated CR-CG offsets are given in µm, and the slider commands and encoder positions are given in degrees.

Iter.	$\hat{x}_{cg}$ [µm]	$\hat{y}_{cg}$ [µm]	$\hat{z}_{cg}$ [µm]	$\Delta s_{\text{raw},x}$ [deg]	$\Delta s_{\text{raw},y}$ [deg]	$\Delta s_{\text{raw},z}$ [deg]	$\Delta s_{\text{cmd},x}$ [deg]	$\Delta s_{\text{cmd},y}$ [deg]	$\Delta s_{\text{cmd},z}$ [deg]	enc_x [deg]	enc_y [deg]	enc_z [deg]
1	1.5615	1.8100	-265.142	-10.2207	-11.8470	1806.0982	10.2207	11.8470	0	10.044	11.628	0
2	-0.0156	-0.4661	-250.971	0.1020	3.0507	1671.4923	0	0	-360	10.044	11.628	-359.856
3	0.0088	-0.4010	-219.011	-0.0574	2.6250	1367.9145	0	0	-360	10.044	11.628	-719.856
4	0.1030	-0.1940	-165.652	-0.6745	1.2699	861.0744	0	0	-360	10.044	11.628	-1079.86
5	0.7859	-0.0877	-149.482	-5.1442	0.5739	707.4807	0	0	-360	10.044	11.628	-1439.82
6	1.2497	0.1684	-127.977	-8.1797	-1.1021	503.2116	8.1797	1.1021	0	18.180	12.744	-1439.86
7	-0.0128	-0.1532	-127.820	0.0839	1.0029	501.7203	0	0	-360	18.180	12.744	-1799.86
8	0.3035	0.0054	-95.0828	-1.9865	-0.0353	190.7601	0	0	0	18.180	12.744	-1799.86

Table A.2: Detailed FRAMBO balancing records. The estimated CR-CG offsets are given in µm, and the slider commands and encoder positions are given in degrees.

Trial	$\hat{x}_{cg}$ [µm]	$\hat{y}_{cg}$ [µm]	$\hat{z}_{cg}$ [µm]	$\Delta s_{\text{raw},x}$ [deg]	$\Delta s_{\text{raw},y}$ [deg]	$\Delta s_{\text{raw},z}$ [deg]	$\Delta s_{\text{cmd},x}$ [deg]	$\Delta s_{\text{cmd},y}$ [deg]	$\Delta s_{\text{cmd},z}$ [deg]	enc_x [deg]	enc_y [deg]	enc_z [deg]
1	0.2316	0.3934	-84.3363	-1.5157	-2.5751	563.6170	0	0	-338.1700	0	0	-338.184
2	0.9817	3.7124	-190.9290	-6.4257	-24.2996	1576.1100	6.4257	24.2996	0	6.408	24.228	-338.184
3	-2.3233	-7.0698	-69.1763	15.2070	46.2752	419.6170	-7.6035	-23.1376	0	-0.972	1.404	-338.184
4	-0.0652	0.4231	-60.2105	0.4268	-2.7693	334.4540	0	0	-200.6724	-0.972	1.404	-538.814
5	0.0958	0.6867	-42.3175	-0.6271	-4.4945	164.4940	0	0	-49.3481	-0.972	1.404	-587.810
6	0.0207	1.2984	-33.3349	-0.1354	-8.4986	79.1702	0	4.2493	0	-0.972	5.328	-587.810
7	-0.1358	0.0075	-36.8673	0.8891	-0.0490	112.7240	0	0	-33.8171	-0.972	5.328	-621.542
8	0.2929	0.3646	-33.6496	-1.9175	-2.3862	82.1594	0	0	-24.6478	-0.972	5.328	-646.094
9	0.6119	0.7235	-30.3074	-4.0053	-4.7358	50.4133	2.0027	2.3679	0	1.116	7.678	-646.094
10	0.0848	0.0938	-23.1258	-0.5551	-0.6139	-17.8027	0	0	0	1.116	7.628	-646.094
11	0.0830	0.1146	-27.6205	-0.5432	-0.7502	24.8911	0	0	0	1.116	7.628	-646.094

References

[1] D. Jung, P. Tsiotras, A 3-dof experimental test-bed for integrated attitude dynamics and control research, in: AIAA Guidance, Navigation, and Control Conference and Exhibit, Austin, Texas, 2003, AIAA Paper 2003-5331. doi:10.2514/6.2003-5331.

[2] D. Thomas, A. T. Wolosik, J. Black, Cubesat attitude control simulator design, in: AIAA Modeling and Simulation Technologies Conference, Kissimmee, Florida, 2018, AIAA Paper 2018-1391. doi:10.2514/6.2018-1391.

[3] R. C. da Silva, R. A. Borges, S. Battistini, C. Cappelletti, A review of balancing methods for satellite simulators, Acta Astronautica 187 (2021) 537–545. doi:10.1016/j.actaastro.2021.05.037.

[4] J. Prado, G. Bisiacchi, L. Reyes, E. Vicente, F. Contreras, M. Mesinas, A. Juarez, Three-axis air-bearing based platform for small satellite attitude determination and control simulation, Journal of Applied Research and Technology 3 (3) (2005) 222–237. doi:10.22201/icat.16656423.2005.3.03.563.

[5] M. A. Peck, L. Miller, A. R. Cavender, M. Gonzalez, T. Hintz, An airbearing-based testbed for momentum-control systems and spacecraft line of sight, in: 13th Annual AAS/AIAA Space Flight Mechanics Meeting, Vol. 114 of Advances in the Astronautical Sciences, 2003, pp. 427–446, AAS Paper 03-127.

[6] N. Jovanovic, J. M. Pearce, J. Praks, Design and testing of a low-cost, open source, 3-D printed air-bearing-based attitude simulator for CubeSat satellites, Journal of Small Satellites 8 (2) (2019) 859–880. URL https://jossonline.com/wp-content/uploads/2021/08/Final-Jovanovic-Design-and-Testing-of-Low-Cost-Open-Source-3-D-Printed-Air-Bearing-Based-Attitude-Simulator-for-CubeSat-Satellites.pdf

[7] L. O. Inumoh, J. L. Forshaw, N. M. Horri, Tilted wheel satellite attitude control with air-bearing table experimental results, Acta Astronautica 117 (2015) 414–429. doi:10.1016/j.actaastro.2015.09.007.

[8] J. J. Kim, B. N. Agrawal, Automatic mass balancing of air-bearing-based three-axis rotational spacecraft simulator, Journal of Guidance, Control, and Dynamics 32 (3) (2009) 1005–1017. doi:10.2514/1.34437.

[9] S. Chesi, Q. Gong, V. Pellegrini, R. Cristi, M. Romano, Automatic mass balancing of a spacecraft three-axis simulator: Analysis and experimentation, Journal of Guidance, Control, and Dynamics 37 (1) (2014) 197–206. doi:10.2514/1.60380.

[10] J. P. Contreras, N. A. Arestegui, E. H. Cayo, E. M. Pumacota, Low weight and inertia self-balancing testbed for a 3u cubesat attitude control system, IEEE Access 13 (2025) 140392–140411. doi:10.1109/ACCESS.2025.3597232.

[11] R. Boynton, Using a spherical air bearing to simulate weightlessness, in: 55th Annual Conference of the Society of Allied Weight Engineers, 1996, SAWE Paper No. 2297.
URL https://raptor-scientific.com/content/uploads/2020/10/Using_a_Spherical_Air_Bearing_to_Simulate_Weightlessness.pdf

[12] Y. Li, Y. Gao, Equations of motion for the automatic balancing system of 3-dof spacecraft attitude control simulator, in: 2010 3rd International Symposium on Systems and Control in Aeronautics and Astronautics, IEEE, Harbin, China, 2010, pp. 248–251. doi:10.1109/ISSCAA.2010.5633650.

[13] G. Di Domenico, F. Topputo, Disturbances quantification for air-bearing spacecraft attitude simulation platforms, in: AIAA SCITECH 2024 Forum, 2024, AIAA Paper 2024-0379. doi:10.2514/6.2024-0379.

[14] A. Bahu, D. Modenini, Automatic mass balancing system for a dynamic cubesat attitude simulator: development and experimental validation, CEAS Space Journal 12 (4) (2020) 597–611. doi:10.1007/s12567-020-00309-5.

[15] Z. Xu, N. Qi, Y. Chen, Parameter estimation of a three-axis spacecraft simulator using recursive least-squares approach with tracking differentiator and extended kalman filter, Acta Astronautica 117 (2015) 254–262. doi:10.1016/j.actaastro.2015.08.010.

[16] A. R. Krishnanunni, S. Jayadevan, A. Mony, G. N. Sharma, Inertia and center of mass estimation of a 3 DoF air bearing platform, IFAC-PapersOnLine 51 (1) (2018) 219–224. doi:10.1016/j.ifacol.2018.05.047.

[17] A. Curatolo, A. Bahu, D. Modenini, Automatic balancing for satellite simulators with mixed mechanical and magnetic actuation, Aerospace 9 (4) (2022) 223. doi:10.3390/aerospace9040223.

[18] Y. Liu, L. Li, Z. Fu, J. Tan, K. Li, Automatic mass balancing of a spacecraft simulator based on non-orthogonal structure, in: 2016 UKACC 11th International Conference on Control (CONTROL), IEEE, Belfast, UK, 2016, pp. 1–6. doi:10.1109/CONTROL.2016.7737579.

[19] B. Wie, H. Weiss, A. Arapostathis, Quaternion feedback regulator for spacecraft eigenaxis rotations, Journal of Guidance, Control, and Dynamics 12 (3) (1989) 375–380. doi:10.2514/3.20418.

[20] B. Wie, Space Vehicle Dynamics and Control, 2nd Edition, American Institute of Aeronautics and Astronautics, Reston, Virginia, 2008. doi:10.2514/4.860119.

[21] VectorNav Technologies, VN-100 IMU/AHRS (2026).
URL https://www.vectornav.com/products/detail/vn-100

[22] Physik Instrumente, A-65x Series Air Bearing Rotation Stages Datasheet (2026).
URL https://www.pikorea.co.kr/fileadmin/user_upload/physik_instrumente/files/datasheets/A-65x-Datasheet.pdf

[23] WITMotion, BWT901CL Bluetooth 2.0 9-Axis Gyro Angle Magnetic Sensor (2026).
URL https://witmotion-sensor.com/collections/all/products/bluetooth-2-0-9-axis-gyro-angle-magnetic-sensor-bwt901cl

[24] maxon motor, EC 45 flat, Brushless, 30 Watt Datasheet (2021).
URL https://www.maxongroup.co.kr/medias/sys_master/root/8882562924574/EN-21-295.pdf

[25] maxon motor, EPOS4 Module/Compact 50/5 Positioning Controller Hardware Reference (2025).
URL https://www.maxongroup.co.kr/medias/sys_master/root/9444048273438/EPOS4-Module-Compact-50-5-Hardware-Reference-En.pdf

[26] maxon motor, Encoder MILE 256–2048 CPT, 2 Channels, with Line Driver Datasheet (2021).
URL https://www.maxongroup.co.kr/medias/sys_master/root/8883954745374/EN-21-460-461.pdf

[27] Leadshine, iCS-RS1706 Integrated Closed Loop Stepper Motor (2026).
URL https://www.leadshine.com/product-detail/iCS-RS1706.html

[28] D. Jung, P. Tsiotras, An experimental comparison of CMG steering control laws, in: AIAA/AAS Astrodynamics Specialist Conference and Exhibit, Providence, Rhode Island, 2004, AIAA Paper 2004-5294. doi:10.2514/6.2004-5294.